CH4 Steam Reforming on Pt+Pd/Al2O3 Monolith: Impact of Mn0.5Fe2.5O4 Spinel Addition

Journal:	*Catalysis Science & Technology*
Manuscript ID	CY-ART-02-2022-000270
Article Type:	Paper
Date Submitted by the Author:	10-Feb-2022
Complete List of Authors:	Chen, Pak Wing; University of Houston, Chemical & Biomolecular Engineering Maiti, Debtanu; University of Houston, Chemical & Biomolecular Engineering Liu, Ru-Fen; University of Houston, Chemical & Biomolecular Engineering Grabow, Lars; University of Houson, Chemical and Biomolecular Engineering Harold, Michael; University of Houston, Chemical & Biomolecular Engineering

SCHOLARONE™
Manuscripts

CH$_4$ Steam Reforming on Pt+Pd/Al$_2$O$_3$ Monolith:

Impact of Mn$_{0.5}$Fe$_{2.5}$O$_4$ Spinel Addition[†]

Pak Wing Chen[1], Debtanu Maiti[1],

Ru-Fen Liu[2], Lars C. Grabow[1]*, Michael P. Harold[1]*

[1]William A. Brookshire Department of Chemical and Biomolecular Engineering,

University of Houston, Houston, Texas 77204, USA

[2]CDTi Advanced Materials, Inc., 1641 Fiske Place, Oxnard, California 93033, USA

*Corresponding author: grabow@central.uh.edu; mpharold@central.uh.edu

[†]Electronic supplementary information (ESI) available

ABSTRACT

The performance of Pt+Pd/Al$_2$O$_3$ monolith catalysts was analyzed under a feed (H$_2$+CO+CH$_4$+NO+O$_2$+H$_2$O+CO$_2$) simulating the exhaust gas of stoichiometric natural gas vehicles (NGVs). The flow reactor results show enhanced low temperature (< 400°C) CH$_4$ oxidation activity under cyclic lean/rich feed modulation and with Mn$_{0.5}$Fe$_{2.5}$O$_4$ (MFO) spinel addition to the platinum group metal (PGM) catalyst. In the absence of the MFO spinel, the PGM catalyst can achieve full CH$_4$ conversion, but the presence of spinel in the catalyst limits the high temperature (> 500°C) CH$_4$ conversion. The depletion of gas phase O$_2$, as indicated by the detection of products CO and H$_2$ in the reactor effluent at higher temperature and CH$_4$ conversion, portends the emergence of steam reforming of CH$_4$ (SRM). To investigate the cause of the detrimental impact of spinel under the high temperature, net rich regime, we show through a combination of SRM experiments and post-reaction catalyst characterization that SRM is negatively impacted by the accumulation of Mn and Fe spinel species on the PGM catalyst. This is due to the migration of the base metal species and potential encapsulation and blockage of PGM active sites. The latter is supported by density functional theory (DFT) calculations that indicate favorable metal oxide decoration of active Pt step sites. Finally, a zoned catalyst design is developed that mitigates the detrimental metals migration while exploiting the methane conversion enhancement afforded by spinel oxides under oxygen rich conditions.

1. INTRODUCTION

Natural gas vehicles (NGVs) are a potentially attractive alternative to gasoline vehicles, leveraging the abundance of inexpensive natural gas due to advances in hydraulic fracturing technology.[1] Distinct advantages of NGVs include lower CO_2 emissions as a result of the higher H:C fuel ratio and the lower cost of natural gas compared to petroleum-based diesel or gasoline.[1,2] Further, stoichiometric natural gas engines operation allows for a simpler NO_x reduction strategy, compared to lean burn engines which require costly urea-based selective catalytic reduction (SCR).

The current technology used for stoichiometric NGV emission control consists of a platinum group metal (PGM) based three-way catalyst (TWC) containing an oxygen storage material (OSM) component. The widely-used OSM, ceria-zirconia (CZO), readily undergoes redox cycling, and acts as an oxygen buffer during fluctuations in the lean-rich ratio. Because of their tunable oxygen storage properties, there is growing interest in using transition metal oxides as well as mixed metal oxides to improve TWC performance. Chang and McCarty showed that manganese oxide (MnO) supported on an inert $LaAlO_3$ perovskite can be added to the conventional TWC to enhance reduction of NO and oxidation of CO and CH_4.[3] Golden et al. reported that Cu-Mn based spinel exhibits exceptional oxygen storage capacity (OSC), and with its incorporation in a Pd-based TWC, resulting in higher catalyst activity for NO_x and hydrocarbons (HC) removal. The spinel addition also reduces the required PGM loading in the catalyst formulation.[4]

Standard operation of stoichiometric NGVs leads to fluctuations in the exhaust composition. This modulation of the air-fuel ratio can be ascribed to feedback from the oxygen sensor-based control system. Due to a time lag, the controller induces periodic changes in the composition of the flow that enters the catalytic converter. Such oscillations can cause rapid lean-rich fluctuations, or dithering, at frequencies as high as 1 Hz. Ferri et al. demonstrated that deliberate periodic rich/lean operation obtained by varying the O_2 concentration in the feed gas leads to enhanced CH_4 oxidation over a Pd-only TWC.[5] Similarly, our group has recently reported enhanced CH_4 conversion under lean/rich modulation of a net rich feed over a $Pt+Pd/Al_2O_3$ monolith with the $Mn_{0.5}Fe_{2.5}O_4$ (MFO) spinel addition.[6] The light-off temperature at 50% CH_4 conversion (T_{50}) is reduced

by ~85ºC with spinel addition under a full feed simulating the NGV exhaust gas. Similarly, Gong et al. reported that the performance of a commercial Pd-based TWC for stoichiometric NGV is higher under a realistic lean/rich cycling condition compared to static operation.[7] The impacts of modulation frequency and amplitude on CH_4 conversion were also reported.

In addition to deep and partial CH_4 oxidation, steam reforming of CH_4 (SRM) is also an important CH_4 conversion pathway given the high H_2O concentration in the exhaust and the potential depletion of gas phase O_2 during modulated operation. The O_2 depletion is encountered at high temperature and CH_4 conversion, indicated by the incremental CH_4 conversion and co-generation of CO and H_2 in the reactor effluent, suggesting participation of SRM. Bugosh et al. revealed through spatially-resolved capillary-inlet mass spectrometry (SpaciMS) measurements during net-rich methane oxidation on a Pt-Pd/Al_2O_3 coated monolith catalyst the co-existence of a front oxidation zone and a downstream reforming zone. Beyond the point of O_2 depletion both CO and H_2 are produced while additional CH_4 is consumed. While CH_4 partial oxidation cannot be ruled out upstream, the downstream concentration profiles imply a combination of steam reforming and water gas shift (WGS) reactions.[8] Salaün et al. reported that WGS and CH_4 steam reforming on a commercial NGV exhaust catalyst act as important reactions at high temperature. On the other hand, dry reforming ($CH_4 + CO_2$) is not likely as it is too slow to compete with steam reforming. [9]

In this study we delve more deeply into the role of MFO spinel on CH_4 steam reforming over the PGM monolith catalyst. To remove contributions from other reactions that occur under the application-relevant feed, the catalyst performance of CH_4 steam reforming under a simpler feed (CH_4+H_2O) is evaluated separately. A detrimental effect of MFO spinel is observed on steam reforming activity. While a PGM monolith catalyst can achieve full CH_4 conversion, the addition of spinel to the catalyst leads to a drop in CH_4 conversion at high temperature. The cause of the CH_4 conversion inhibition is investigated through post-steam reforming catalyst characterization and density function theory (DFT) calculations. Finally, a prospective catalyst zoning design is proposed that can help mitigate the unfavorable effect of spinel on CH_4 conversion under the NGV

exhaust gas reaction conditions. The findings have important implications for the design of catalytic converters to treat exhaust from stoichiometric combustion NGVs.

2. MATERIALS AND METHODS

2.1 Catalysts

All cordierite monolith samples were provided by CDTi Advanced Materials, Inc. (Oxnard, CA) and their compositions and architectures are summarized in Table 1. All monolith samples have a 600 cpsi (cells per square inch) cordierite substrate with the same dimension of 1'' (D) and 0.85'' (L). Three types of washcoated monolith samples are depicted in Fig. 1a. The PGM+Spinel catalyst denoted by 30/100/25 comprises a PGM top layer and the bottom spinel layer both having total material washcoat loadings of 100 g/L monolith. The PGM-containing layer has a composition of 1.06 wt.% PGM/Al_2O_3 (19:1 Pt:Pd mass ratio) and an overall 30 g PGM/ft^3 metals loading. The 100 g/L spinel layer contains dispersed $Mn_{0.5}Fe_{2.5}O_4$ with a mass fraction of 25 wt.% on Al_2O_3. Similarly, the PGM-Only catalyst (30/100a) has the same dual-layer structure but the spinel alumina layer is replaced by an Al_2O_3-only layer with a loading of 100 g/L. The Spinel-Only catalyst (0/100/25) consists of a single layer of MFO spinel on Al_2O_3 with the same 25 wt.% spinel mass loading. A single-layer monolith sample depicted in Fig. 1b was also tested. This mixed washcoat sample (denoted as 30/100/25-PM) has the same loadings of components as its dual-layer counterpart. The sample was prepared by physically mixing the 1.06 wt.% PGM/Al_2O_3 powder and 25 wt.% $Mn_{0.5}Fe_{2.5}O_4$/Al_2O_3 powder with deionized (DI) water, forming into a slurry solution that was ball-milled before the washcoating process. As such, this sample is considered to have the PGM component in closer proximity to the spinel component than the dual-layer sample. To examine the effect of total washcoat loading, monolith samples with reduced spinel layer loading of 60 g/L were also tested. The spinel loadings vary from 7.5 g/L to 15 g/L. A PGM-Only (30/60a) with 60 g/L of alumina layer was included for comparison. Schematics of these samples are shown in Fig.1c. Finally, another PGM+Spinel sample 30/140/35, depicted in Fig.1d, was included in the catalyst zoning study. This sample has the same PGM top layer as the other samples mentioned above, but has a 140 g/L spinel layer loading. The mass fraction of the spinel layer is the same 25 wt.%, thus yielding 35 g/L spinel loading. The 1.06 wt.%

PGM/Al$_2$O$_3$ powder and 25 wt.% Mn$_{0.5}$Fe$_{2.5}$O$_4$/Al$_2$O$_3$ powder sample that were used for washcoating the monolith samples were also provided by CDTi Advanced Materials, Inc.

2.2 Catalyst Characterization

2.2.1 Full feed flow experiments

The flow experiments were conducted in the same bench reactor system described in our previous work.[6] To simulate the exhaust from a stoichiometric NGV, an application-relevant "full" feed composed of CH$_4$, H$_2$, CO, NO, O$_2$, H$_2$O, CO$_2$ and inert carrier N$_2$ was used. The concentration of each species is listed in Table 2. The parameter Lambda (λ) defined by

$$\lambda = \frac{0.5\left[(CO) + 2(O_2) + (NO) + (H_2O) + 2(CO_2)\right]}{\left[(CO) + (CH_4) + (CO_2)\right] + 0.25\left[2(H_2) + 4(CH_4) + 2(H_2O)\right]} \tag{1}$$

is used to characterize the lean/rich ratio of the full feed. The λ definition considers species containing O to be oxidants and species containing H and C to be reductants. Two feed gas conditions were used, time-invariant (λ = 0.992) and modulated feed (λ = 0.978-1.006). The concentration of each gas species was held constant for the time-invariant feed, while for the modulated feed the O$_2$ concentration was switched between a lower rich value to a higher lean value every 1.5 sec, corresponding to a period of 3 sec and a modulation frequency of 0.33 Hz.

Throughout the entire study the gas hourly space velocity (GHSV) was set at 40,000 h^{-1} (@ STP), corresponding to a total volumetric flow rate of 7.2 standard L/min. The effluent concentrations of CH$_4$, CO, NO, H$_2$O and CO$_2$ were measured using a FTIR (MKS model MultiGas 2030) while the H$_2$ concentration was measured using a mass spectrometer (MS, MKS model Cirrus 1). The effluent gas during multiple cycles encounters a T-section with one side leading to a FTIR and the other side leading to the capillary of the MS. This design enabled measurement of the effluent by both FTIR and MS simultaneously. The full feed experiments were conducted at a set of fixed feed temperatures between 105°C and 600°C. The reported data were obtained once the effluent gas concentrations were constant, typically after 20-30 minutes. For the modulated feed experiments, the cycle-averaged conversion is reported.

Before each experiment, a pretreatment in 3% O_2 in balance N_2 was conducted at 550°C for 30 min on all catalysts to remove air and moisture in the reactor system.

2.2.2 CH$_4$ steam reforming

A set of experiments were conducted to examine the effect of spinel on the PGM CH$_4$ steam reforming activity. These involved temperature-ramp SRM experiments with monolith catalysts having varying degrees of proximity between the PGM and spinel components along with different spinel loadings. The concentrations of CH$_4$ and H$_2$O were kept constant as per the full feed composition. The temperature ramp rate was 5°C/min and the pretreatment procedure were the same as the pretreatment described in section 2.2.1.

2.2.3 Diffuse reflectance infrared Fourier transform spectroscopy

Diffuse reflectance infrared Fourier transform spectroscopy (DRIFTS) experiments were carried out to characterize the surface species on the PGM top layer of the monolith catalysts before and after the steam reforming reaction. The monolith catalysts used from the steam reforming experiments were cut in half axially to expose the washcoat. A small monolith piece was cut from the center region of each monolith sample. The samples were cut carefully such that PGM overcoat layer remained intact with the spinel layer buried. To fit the sample into the sample holder, the monolith sample was cut into a near circular shape that was 4 channels (~5 mm) in diameter and 1 channel (~1 mm) deep.

The DRIFTS measurements were conducted using a Nicolet model 6700 FTIR spectrometer (Thermo-Scientific) equipped with a sample holder (Harrick Scientific Products). The samples were first pretreated in inert Ar atmosphere at 550°C for 1 hr before being cooled in Ar to 25 °C. After pretreatment, the background was collected, and the sample was treated with 10% CO in balance Ar for 1 hr at 25°C. The sample holder was subsequently purged with Ar for 1 hr. During the CO saturation and Ar purging stages, the IR spectra with the range of 4000 to 1000 cm^{-1} were taken every 2 min. Each spectrum has a resolution of 1.928 cm^{-1} and was averaged over 15 scans. The feed gas was controlled by Bronkhorst mass flow controllers, with a total flow rate of 60 ml/min. The presented spectra of the CO saturation and Ar purging stages for each sample was

obtained after 30 min. No significant difference was seen between all the collected spectra during the 1 hr measurement.

2.2.4 Scanning electron microscopy–energy dispersive X-ray spectroscopy

The samples for the scanning electron microscopy–energy dispersive X-ray spectroscopy (SEM-EDX) were prepared by the same procedure as described in section 2.2.3. After getting the small monolith piece, the sample was further cut such that a flat piece was obtained. For the PGM-Only samples, a JEOL JSM 6400 system at 15 kV and 15 mm working distance was used; for the PGM+Spinel samples, the Phenom Pro Desktop SEM (Thermo-Scientific) instrument operating at 15 kV and 15 mm working distance was used. The elemental concentrations and detailed elemental mapping analyses were used to characterize the top PGM layer. For all the PGM+Spinel or PGM-Only samples, the SEM images were obtained with the same resolution and the elemental mapping analyses were conducted on the similar washcoat sizes. The atomic concentrations of the elements were averaged based on the washcoat area chosen.

2.2.5 Computational Methodology

Periodic, spin-polarized density functional theory (DFT) calculations were performed to investigate the thermodynamic driving force for migration and encapsulation of the Pt(211) and Pt(111) surfaces with binary metal oxides and hydroxide species (MO_xH_y). The Vienna ab-initio Simulation Package (VASP) along with the Atomic Simulation Environment (ASE) was used for this purpose.[10–14] All calculations were based on the projector augmented wave (PAW) methodology of core and valence electron representation.[15,16] The van der Waals corrected Bayesian error estimation functional (BEEF-vdW) was used to describe exchange and correlation effects.[17] The wave function was expanded into a plane wave basis set using a kinetic energy cutoff of 500 eV. Gaussian smearing with a Fermi temperature of k_bT = 0.1 eV was used with subsequent extrapolation of electronic energies to k_bT = 0.0 eV.

For the high index Pt(211) facets, we studied the possibility of metal oxide and hydroxide adsorption on the terrace and step sites. Embedding of MO_xH_y on Pt(211) was also probed whereby a surface Pt atom is replaced with a Fe or Mn atom. The optimized Pt

bulk lattice constant, as obtained by the BEEF-vdW functional, is 3.99 Å, which is in good agreement with the experimental value of 3.91 Å.[18] The Pt(211) facet was modelled as a four layer (3×1) supercell consisting of 36 Pt atoms. Consecutive slabs were separated in the z-direction with a vacuum distance of 16 Å. While the bottom two layers were fixed to their bulk lattice positions, the top two atomic layers were allowed to relax and reconstruct until the residual forces converged to below 0.02 eVÅ^{-1}. A Gamma centric (4×6×1) k-point mesh was used to sample the Brillouin zone, and a dipole correction to the electrostatic potential along the z-direction was applied.[19]

The heat of MO_xH_y adsorption on Pt(hkl) (Equation 2) was calculated on a per migrant metal atom basis with reference to Pt(hkl), Pt(bulk), the respective binary MO(bulk), and H_2(gas).

$$m \times E_{ads} = E[MO_xH_y \, on \, Pt(hkl)] - E[Pt(hkl)] - mE[MO(bulk)] + pE[Pt(bulk)] - h\frac{E[H_2(gas)]}{2} \qquad (2)$$

MO_xH_y on Pt(hkl) consists of m units of metal oxide (MO), h H atoms along with p atoms of Pt dislodged during MO_xH_y embedding in Pt(hkl).

For Pt(111) encapsulation with FeO, experimental and theoretical studies have identified a characteristic $(\sqrt{91} \times \sqrt{91})R5.2°$ superlattice as preferred structure for FeO(111)/Pt(111).[20–22] Moreover, the presence of strong reducing agents such as CO induces Fe_3O_2 film formation on Pt(111) facets, leading to a (2×2) overlayer structure. Thus, we investigated the energetics of 1 ML FeO and FeOH on a 3-atomic layer thick ($\sqrt{91} \times \sqrt{91})R5.2°$ unit cell and Fe_3O_2 on a (2×2) unit cell of Pt(111). The bottom two layers were fixed to their bulk lattice configuration, while allowing the top Pt and FeO_xH_y layers to fully relax.

3. RESULTS AND DISCUSSION

3.1 Role of spinel on CH$_4$ oxidation during lean/rich feed modulation

The performance of three catalysts, PGM+Spinel (30/60/15), PGM-Only (30/60a), and Spinel-Only (0/60/15) were first assessed using the composition simulating NGV exhaust under two feed conditions, time-invariant and modulated. While similar experiments were conducted in our earlier work[6], the new measurements reported here provide for an expanded assessment for the same samples evaluated subsequently for SRM activity.

The CH$_4$ conversion data under time-invariant feed (dashed lines) and modulated feed (solid lines) for the three catalysts are shown in Fig. 2. The Spinel-Only catalyst has negligible activity for temperatures below 500ºC (purple triangles) for both feed conditions. In contrast, the PGM-Only catalyst (red circles) is active for converting CH$_4$, with feed modulation shown to have a significant beneficial effect as indicated by a reduction in T$_{50}$ from 488ºC to 438ºC. Complete CH$_4$ conversion is achieved at 570ºC under the modulated feed and 98% CH$_4$ conversion is reached at 588ºC under the time-invariant feed.

Enhancement of CH$_4$ oxidation by feed modulation has been previously reported. Carlsson et al. studied the influence of periodic operation on CH$_4$ conversion for Pt/Al$_2$O$_3$ and Pd/Al$_2$O$_3$ monolith catalysts. Enhanced CH$_4$ conversion was observed for Pt/Al$_2$O$_3$ by varying the O$_2$ feed concentration but not for Pd/Al$_2$O$_3$.[23] The Pd catalyst instead exhibited a higher CH$_4$ conversion activity under a continuous oxidizing feed than under periodic operation with O$_2$ pulsing. These findings suggest that the optimal O$_2$ concentrations over Pt and Pd crystallites are different. Fouladvand et al. reported that increasing the concentration of oxygen decreases the conversion of CH$_4$ over a Pt/Al$_2$O$_3$ catalyst but the adverse effect of excess O$_2$ could be circumvented through periodic operation.[24] They suggested that O$_2$ inhibits the dissociative adsorption of CH$_4$, resulting in a lower reaction rate. For the Pt-rich PGM catalysts used in our previous[6] and current study, the data reveal enhanced CH$_4$ conversion under feed modulation and net rich conditions. Collectively, these observations suggest that cyclic lean/rich switching may lead to dynamically formed active sites on the PGM surface for enhanced CH$_4$ dissociation even in the absence of an oxygen storage function.

The observed decrease in activity under steady oxidizing treatment is attributed to surface oxidation of Pt. Using in situ X-ray photoelectron spectroscopy (XPS), Pakharukov et al. claimed that metallic Pt is the responsible active phase for CH_4 activation while the oxidized Pt is less active.[25] In another study using in situ X-ray absorption spectroscopy (XANES, EXAFS), the authors reported that changes in the Pt electronic state under high and low CH_4 oxidation activity regimes are attributable to changes in the O/Pt surface ratio.[26] Detailed experimental and DFT studies in different kinetic regimes observed during CH_4 oxidation on Pt clusters were conducted by Chin et al.[27] Over a partially oxygen covered surface with exposed Pt atoms, the C-H bond activation on the Pt-PtO site pair leads to higher turnover rates than on PtO-PtO and Pt-Pt site pairs. The synergistic role of Pt-PtO comes from the lower C-H bond activation barrier on Pt and the subsequent H abstraction by O to form Pt-OH. Thus, Pt surface with an intermediate oxygen coverage is favored for CH_4 oxidation activity.

Ceria is a widely-used OSM in PGM-based TWC emission control catalysts. It has been shown to improve CH_4 oxidation activity. Becker et al. explained that the higher CH_4 oxidation activity over Pt/CeO_2 compared to Pt/Al_2O_3 is due to the high OSC/oxygen mobility of/in CeO_2.[28] The higher OSC of the Pt/CeO_2 catalyst also leads to more resilience to oxygen poisoning, enabled by the ability of CeO_2 to buffer oxygen, storing some of the excess oxygen during a lean feed. This creates vacant Pt sites for CH_4 adsorption and dissociation. Another explanation for enhanced CH_4 oxidation activity is that ceria provides sites at the $Pt-CeO_2$ interface for CH_4 dissociation. These two mechanisms both require close proximity of ceria to Pt.

In the current study, the presence of MFO spinel similarly leads to enhanced CH_4 oxidation activity. Fig. 2 compares the PGM-Only and dual-layer PGM+Spinel catalysts. The addition of MFO spinel to PGM (black squares) resulted in a lower T_{50} for CH_4 conversion under both a modulated feed (~50ºC reduction) and a time-invariant feed (~15ºC reduction). These data corroborate our earlier findings.[6] The MFO spinel was compared to the widely-used CZO as the OSM in the dual function catalyst. To examine the OSM proximity issue, the PGM+Spinel and PGM+CZO (as $Ce_{0.3}Zr_{0.7}O_2$) both have the dual-layer design and identical PGM and OSM loadings (25 wt.% OSM on Al_2O_3).

Their CH_4 conversion profiles under the modulated and time-invariant feed conditions are shown in Fig. S1a in the Supplementary Information (SI). A higher CH_4 conversion was obtained for the MFO sample up to 430°C and 490°C under modulated and time-invariant feed, respectively. However, the PGM+CZO sample outperforms the PGM+Spinel catalyst at the higher temperature SRM regime.

These findings collectively suggest that the spinel effectively promotes the CH_4 oxidation activity of the PGM in the lower temperature regime since the Spinel-Only catalyst is only active for CH_4 conversion at temperature above 500°C (Fig. 2). On the other hand, Spinel-Only catalyst is active for CO and H_2 oxidation starting from 285°C under both modulated and time-invariant feed conditions (not shown here). As for CZO, its beneficial impact is attributed to its OSC property. Conversely, the MFO spinel provides enhanced activity despite its location in a separate, albeit contiguous layer. This suggests a kinetic coupling between the PGM and OSM through the gas phase rather than on the surface. This could be enabled through O_2 diffusion to and removal by the MFO spinel layer, maintaining the PGM surface in a partially oxidized state for enhanced CH_4 activation. The enhancement might also be a result of the diffusion of methane partial oxidation or reforming products CO and H_2 to the spinel layer where they are oxidized. Finally, the clear performance differences between the MFO spinel and CZO indicate that the choice of OSM depends on the temperature regime and availability of O_2. We expand on these points below.

### 3.2 Evidence for steam reforming under high-temperature full feed condition

Under the full feed condition, oxidation and reforming chemistries both contribute to CH_4 conversion. Deep oxidation of CH_4 occurs in the presence of O_2:

$$CH_4 + 2O_2 \rightarrow CO_2 + 2H_2O \tag{R1}$$
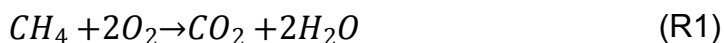
Steam reforming of CH_4 reaction occurs with the high H_2O feed concentration of NGV exhaust:

$$CH_4 + H_2O \leftrightarrow CO + 3H_2 \tag{R2}$$
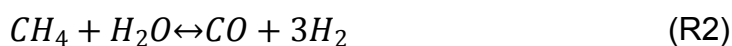
An alternative source of CO and H_2 is via CH_4 partial oxidation:

$$CH_4 + 0.5O_2 \leftrightarrow CO + 2H_2 \qquad (R3)$$
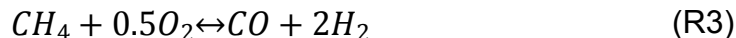
The CO/H_2 reductant ratio is affected by the water gas shift (WGS) reaction:

$$CO + H_2O \leftrightarrow CO_2 + H_2 \qquad (R4)$$

In addition to CH_4 oxidation, other reactions, including the oxidations of H_2, CO may occur:

$$H_2 + 0.5O_2 \rightarrow H_2O \qquad (R5)$$

$$CO + 0.5O_2 \rightarrow CO_2 \qquad (R6)$$

It is noted that only three of these six reactions are linearly independent.

In the current study, experimental evidence for SRM activity was obtained for two catalysts, PGM+Spinel (30/60/15) and PGM-Only (30/60a), under both time-invariant and modulated full feed conditions. The effluent O_2 concentration profile can be predicted based on the measured conversions of CH_4, CO, H_2, and NO and formation of NO_2, NH_3 and N_2O.[6] Figs. S2a, S2b show the latter data. The analysis reveals complete conversion of both CO and H_2 at ~280ºC for the PGM+Spinel (30/60/15) catalyst and at ~340ºC for the PGM-Only (30/60a) catalyst (Fig. 3a) under the time-invariant feed. Under modulating feed conditions CO and H_2 were completely consumed at the lower temperature of ~275ºC for the PGM+Spinel catalyst and at ~330ºC for the PGM-Only catalyst (Fig. 3c).

CO and H_2 formation was observed in the high temperature regime for both catalysts as highlighted by the blue shaded region in Figs. 3a and 3c. Their formation indicates CH_4 steam reforming or partial oxidation. Depletion of O_2 is estimated to occur at about the same temperature at which CO and H_2 formation commence (Figs. 3b and 3d). This rules out partial oxidation as the source for CO and H_2. For the PGM-Only (30/60a) catalyst, complete CH_4 conversion was reached at 570ºC under modulated feed and 98% CH_4 conversion was achieved at 588ºC under time-invariant feed. The addition of MFO to the PGM catalyst results in a lowering of the T_{50} for CH_4 conversion under both time-invariant and modulated feed conditions, as described earlier (section 3.1). However, the high temperature CH_4 conversion levels off at 88% with time-invariant feed and 94% with

modulated feed. These observations suggest that MFO plays a significant role in the high temperature anaerobic catalyst activity.

3.3. Effect of MFO spinel on CH$_4$ steam reforming

To better understand the CH$_4$ reforming chemistry and specifically the role of MFO spinel, a series of temperature-programmed CH$_4$ steam reforming experiments were conducted for a feed containing only CH$_4$, H$_2$O, and N$_2$. The effects of two catalyst properties, the loading of spinel and the proximity between PGM and spinel components, were examined.

The SRM results of the three PGM+Spinel catalysts with different MFO loadings (7.5 g/L to 15 g/L) are compared in Fig. 4a. The PGM-Only catalyst (30/60a) serves as the reference. The T$_{50}$ values for each of the three PGM+Spinel catalysts are higher than the T$_{50}$ (368ºC) for the PGM-Only (30/60a) catalyst. The T$_{50}$ for the PGM+Spinel increases with the spinel loading (375ºC to 388ºC). This suggests an unfavorable effect of the spinel on the PGM steam reforming activity. For the PGM+Spinel catalyst having the highest spinel loading (30/60/15), a small decrease in the CH$_4$ conversion was detected above 500ºC before the end of the temperature ramp at 540ºC. This amounts to a 2% decrease in the CH$_4$ conversion over a period of 6.5 minutes. To examine this further, we evaluated the steam reforming activity at a constant elevated temperature for the same PGM+Spinel catalyst (30/60/15). Prolonged high-temperature CH$_4$ steam reforming activity at constant 550ºC for 90 min showed a gradual decline in CH$_4$ conversion from 94% to 50% as indicated in Fig. 4b. This decline in the catalyst activity is discussed in more detail in section 3.4.

The CH$_4$ steam reforming activity for another group of catalysts were evaluated; namely, PGM-Only (30/100a), Spinel-Only (0/100/25), and PGM+Spinel (30/100/25, 30/100/25-PM). The comparative performance of these catalysts is shown in Fig. 4c. Compared to the PGM-Only catalyst (30/100a), the addition of 25 g/L spinel in a separate washcoat (30/100/25) significantly reduced the PGM steam reforming activity. A nearly 50% drop in CH$_4$ conversion was observed over the temperature range from 470 to 540ºC, which comprised a time period of 14 minutes. This is clear evidence of rapid catalyst

deactivation. The presence of spinel, at the same loading of 25 g/L but in more intimate contact with PGM (30/100/25-PM) worsened the activity decline. Fig. 4c shows that a much lower maximum CH_4 conversion of 58% was observed along with a steeper drop in CH_4 conversion to ~10% from 450°C to 530°C. These data lead to two conclusions: (1) increase of spinel loading from 15 g/L to 25 g/L significantly decreases the PGM activity for SRM; (2) close proximity of PGM and spinel components promotes catalyst deactivation.

The SRM performance of the PGM+Spinel (30/100/25) catalyst is also compared with the PGM+CZO catalyst, which has the same PGM and OSM loadings. The loss of activity of the PGM+Spinel catalyst at high temperature was observed as mentioned above, whereas the PGM+CZO catalyst maintained complete CH_4 conversion. (Fig. S1c). The higher SRM activity of the PGM+CZO catalyst explains its better performance at high temperatures under the full feed conditions (Fig. S1a). For both catalysts, SRM dominates in the high temperature regime after O_2 depletion. As indicated by Fig. S1b, O_2 depletes at ~390°C under modulated feed and at ~475°C under time-invariant feed.

To investigate the cause for the loss in CH_4 reforming activity, a carbon balance analysis was carried out on the PGM-Only (30/100a) and PGM+Spinel (30/100/25, 30/100/25-PM) catalyst samples. The percentage of unaccounted-for carbon is given by the integral carbon imbalance over a time range (t_f = final time and t_i = initial time):

$$C\ imbalance\ (\%) = 100\% * \left(\int_{t_i}^{t_f} C_{in} - \int_{t_i}^{t_f} C_{out} \right) / \int_{t_i}^{t_f} C_{in} \qquad (3)$$

The inlet C species is CH_4 and the outlet C species are CH_4, CO and CO_2. The C_{out} is given by the integrated area under the instantaneous concentration profiles for CH_4, CO and CO_2. The CO/CO_2 ratio is the net result of the WGS reaction (R4) or possible reduction of spinel by CO. The estimated C imbalance for each catalyst over the temperature range of 120 to 540°C with 50°C increments are compared in Fig. 5. The PGM-Only catalyst (30/100a) has the highest integral C imbalance. The C imbalance stabilized after 480°C at 11%. It is noted that even with the continuous C uptake of the PGM-Only (30/100a) catalyst, its steam reforming activity sustained 100% CH_4 conversion at high temperature. This suggests that the carbonaceous species did not

accumulate on the active sites and therefore do not adversely impact the PGM activity. The C imbalances for each of the catalysts overlap up to ca. 400 ^{o}C, but further temperature increase leads to lower values and a maximum for the spinel-containing catalysts. Additional characterization is needed to ascertain the nature and the location of the C species on the catalysts.

Since the deactivation profiles cannot be attributed to different coking behavior, additional steam reforming runs were conducted for the PGM+Spinel (30/100/25) catalyst to explore alternative explanations for its loss of activity (Fig. 6). After reaching the end of the temperature ramp in the first steam reforming run, the catalyst was cooled to ~120ºC in the presence of the same feed gas. The second run was then started using the same temperature ramp as before, and subsequently cooled in the steam reforming gas. The cycle was repeated a third time. The continuous CH_4 conversion profile over the three steam reforming runs is shown in Figs. 6a and 6b for the PGM+Spinel catalyst.

A significant drop in the maximum CH_4 conversion after the first run was observed, with a 40% decrease in the maximum CH_4 conversion in the second run. However, the catalyst had a similar light-off and maximum CH_4 conversion in second and third runs, suggesting that the catalytic activity levels off. That is, while the catalyst had a significant activity loss after the first run, the catalyst activity stabilized thereafter. A similar two-cycle experiment was conducted on the same PGM+Spinel catalyst, but the oxidizing gas (3% O_2/N_2) was fed during the cooling step instead of the steam reforming gas. Referring to Fig. S3 in the SI, a CH_4 conversion profile with a maximum value of ~50% was obtained, which is slightly higher than the level obtained in the second run from the first experiment using reforming feed gas during the cooling step (Fig. 6). Further, no CO or CO_2 were detected during the oxidizing, cooling step. Thus, no carbonaceous species were removed from the catalyst, presumably due to the rather low temperature and low O_2 concentration treatment. The CH_4 conversion profiles in the second and third runs will be discussed in more details in section 3.4.

The same three consecutive steam reforming runs were conducted on the PGM-Only (30/100a) catalyst to rule out the possibility that PGM itself deactivates during this treatment. The PGM-Only catalyst was able to achieve full CH_4 conversion, with no CH_4

conversion drop observed during the temperature ramp stage for all three steam reforming runs, as shown in Fig. 6c. This suggests that the drop in the catalyst activity observed in Figs. 6a and 6b is related to the presence of MFO.

Commonly proposed CH_4 steam reforming mechanisms over supported Pt catalysts involve the dissociation of CH_4 into chemisorbed carbon (C*), which is removed by surface oxygen (O*) derived from H_2O.[29,30] The chemisorbed carbon can also be removed by oxygen supplied from the OSM. Mortola et al. studied the activity of Pt for CH_4 steam reforming using a CeO_2-La_2O_3-Al_2O_3 support with varying ceria loadings. Compared to the Pt/Al_2O_3 catalyst, the increase of CH_4 conversion was attributed to the high oxygen mobility of the support, which leads to higher carbon resistance of the catalyst.[31] Spinel as an OSM is expected to promote CH_4 steam reforming activity as well, but in a different mechanism due to its physical separation from the PGM sites in the dual-layer PGM+Spinel catalyst. However, the decline in the steam reforming activity at high temperature suggests additional factors apart from OSC play a role in CH_4 steam reforming.

3.4 Post-steam reforming catalyst characterization

To elucidate changes in surface composition of the PGM-Only (30/100a) and PGM+Spinel (30/100/25) monolith catalysts, pre-steam reforming and post-steam reforming characterizations on the top PGM layer were carried out.

3.4.1 SEM-EDX characterization

Due to difficulties in separating the PGM layer from the spinel layer on the monolith samples, characterization methods were selected such that no modification of the monolith sample was required and only the top PGM layer was probed. From previous studies on monolith sample characterizations, SEM-EDX is a reliable method to determine the morphology of the washcoat, the cross-sectional washcoat thickness, as well as the chemical compositions at specific regions.[32] The purpose of employing SEM-EDX in this study is to detect possible PGM sintering and the species in the PGM layer that have migrated under steam reforming reaction conditions.

Three PGM+Spinel (30/100/25) catalysts with different treatments were compared, including a fresh catalyst, and two post-steam reforming catalysts. One of the post-steam reforming catalysts was exposed to one steam reforming run and the other one was treated with three steam reforming runs. These samples were used to analyze the change in PGM layer with varying exposure to steam reforming conditions. The SEM images and the elemental distribution maps of Pt (yellow), Fe (teal), Mn (purple) for each sample are shown in Fig. 7a. The measured averaged atomic concentration of each element for all the samples are plotted in Fig. 7b. Without being exposed to the steam reforming treatment, low concentrations of Fe (7.5%) and Mn (0.5%) were detected on the fresh catalyst. These traces of Fe and Mn in the PGM layer may be attributed to the synthesis procedure. After one steam reforming experiment, significantly large amounts of Fe (27.9%) and Mn (4.7%) emerged in the PGM layer. Elemental area mappings show an instance of Pt, Fe and Mn appearing at the same location, suggesting possible formation of a spinel or mixed metal oxide cluster in the PGM layer. Traces of Fe were also observed at different locations. For the sample subjected to the three steam reforming runs, even higher concentrations of Fe and Mn were measured, at 44.6% and 8.5%, respectively. Additional spinel or mixed metal oxide clusters and Fe were also detected at different locations. Thus, the SEM-EDX results confirm elemental or oxide cluster migration from the spinel layer to the PGM layer. While the nature of the migrated Fe and Mn species is unknown, we speculate that binary oxides such as FeO, and MnO form during spinel reduction and participate in the migration. The possible migration of Fe and Mn oxides is discussed next.

Another factor that may lead to catalyst activity loss is PGM sintering, as suggested by SEM-EDX measurements of Pt aggregation (Fig. 7a). Two possible sintering mechanisms may occur; sintering under high temperature reducing condition and sintering induced by the migrated base metal species. To explore the first, an analogous SEM-EDX test was done on a fresh and two post-reforming (one or three steam reforming runs) PGM-Only (30/100a) catalysts. The SEM images and the elemental distribution maps of Pt (green) and Al (blue) for each sample are shown in Fig. 7c. The measured average atomic concentration of each of the elements for each sample are shown in Fig. 7d. After exposure to one steam reforming run, no significant change in the Pt distribution was

observed. The increase in the Pt atomic concentration from 0.19% to 0.26% suggests small Pt cluster formation, which may not be detected based on the SEM image. After being treated with three steam reforming runs, clear evidence of Pt aggregation is indicated by the Pt clusters at various locations shown in the SEM image. The Pt atomic concentration increased to 0.32%, suggesting growth in the Pt cluster size on the washcoat surface. However, with the indication of Pt sintering, no CH_4 conversion decrease was observed (Fig. 6c) during the three consecutive steam reforming experiments as discussed in section 3.3. We conclude that Pt sintering is not the reason for the catalytic activity loss observed for the PGM+Spinel case (Figs. 6a and 6b). This leaves base metal species migration is the culprit. The possibility of the migrated species inducing Pt sintering is not explored further in this study.

3.4.2 Metal oxide and hydroxide (MO_xH_y) migration to PGM surfaces

As portrayed in the SEM-EDX data, a substantial increase in the Fe and Mn content was observed in the PGM layer of the monolith catalyst after steam reforming experiments. To examine our hypothesis that spinel decomposition into FeO and MnO under reducing conditions leads to MO_xH_y (M = Fe, and Mn) migration to the PGM layer, we use DFT to calculate the thermodynamic driving force for this process.

Pt(211) is well known for effective catalytic activation of methane, with step sites proving to be better than terrace sites.[33,34] Thus, we have evaluated the adsorption behavior of FeO_xH_y on the terrace site and step sites of Pt(211) (Fig. 8), and found that FeO and FeOH monomers bind significantly stronger at the step edge. The exothermic heats of adsorption of -0.37 eV and -1.80 eV for FeO and FeOH, respectively, indicate that continuous deposition of FeO and FeOH species on active Pt(211) step sites is likely. Complete decoration of the step with linear chains of FeO and FeOH is shown in Fig. 8 and the energy of formation remains favorable. We also considered embedded FeO_xH_y species in Pt(211), whereby a migrating FeO_xH_y monomer substitutes a Pt atom at the edge site. In the case of monomers, substitutional doping results in an additional energy gain. The favorable adsorption characteristics of FeO_xH_y, as monomer and when fully decorating active step edge sites suggest that migrating Fe species during methane steam reforming conditions can effectively block active PGM sites.

An analogous investigation of the adsorption behavior of MnO_xH_y species is shown in Fig. S4 in section 4 of the SI and shows that MnO_xH_y migration is less favorable than FeO_xH_y migration. In fact, the adsorption of MnO is endothermic, but hydroxylated MnOH species may still deposit at the Pt(211) step-sites. The weaker energy of adsorption for MnO_xH_y species compared to that of FeO_xH_y corroborates our experimental observation of higher Fe enrichment at the PGM layer than that by Mn. Decoration and passivation of PGM step sites with FeO_xH_y (or MnO_xH_y) is also consistent with the observed loss in activity of the PGM+Spinel catalyst samples.

While edge sites are expected to dominate the activity for methane dissociation, terrace sites are more prevalent and may contribute to catalytic activity. To further probe the encapsulation of Pt(111) facets by FeO_xH_y, we have investigated the formation of FeO and FeOH monolayers (MLs) on Pt(111) (Fig. 9). Freund and coworkers have shown that strong metal support interactions (SMSI) between Pt and Fe_3O_4 lead to the encapsulation of Pt with FeO monolayers, forming a FeO(111)/Pt(111) overlayer with characteristic moiré structure in a $(\sqrt{91} \times \sqrt{91})R5.2°$ superlattice.[22] Using bulk FeO as reference, we find the formation of FeO(111)/Pt(111) to be slightly endothermic (0.18 eV), but the hydroxylated monolayer is energetically favorable (-0.05 eV). It has also been reported that presence of CO can induce the formation of a reduced Fe_3O_2 overlayer with (2×2) periodicity on Pt(111).[35] We estimated the stability of this surface by assuming that oxygen is removed as CO_2 by CO oxidation, and obtained the approximate energy of formation as 0.19 eV. Overall, our DFT estimates for full encapsulation of Pt with FeO_x are close to thermoneutral such that their stability will be dictated by the reducing or oxidizing potential of the surrounding gas phase.

Collectively, the theoretical estimates of adsorption energies of the postulated migrated MO_xH_y on Pt show that migration of Fe and Mn to PGM is thermodynamically favorable. The substantially higher stability of FeO_xH_y over MnO_xH_y is consistent with the experimentally observed enrichment of the PGM layer with Fe and Mn. Moreover, the preferential adsorption of FeO_xH_y at step edges can explain the lower methane steam reforming activity due to blocking of PGM sites.

3.4.3 CO-DRIFTS characterization

In-situ CO adsorption DRIFTS studies over metals/metal oxide can provide insight on equilibrated adsorbed surface species and transient species, along with their oxidation states.[36,37] For this reason, CO was chosen as the probe molecule to characterize the surface of the PGM layer. The species represented by the peaks were assigned based on literature results. The spectra collected during Ar purge after CO saturation over the fresh catalysts are compared in Fig. 10a. The peaks at 2092 (PGM-Only) and 2094 cm^{-1} (PGM+Spinel) are assigned to Pt-CO; the smaller peaks at 2067 (PGM-Only) and 2073 cm^{-1} (PGM+Spinel) are assigned to CO-Pt-CO. Bands in the range of 1670-1850 cm^{-1} are assigned to bridge CO species.[38,39] For bidentate carbonate, the bands are v(C=O) at 1620-1670 or 1530-1620, $v_a(COO)$ at 1220-1270, $v_s(COO)$ at 1030-1020 or 980-1020 cm^{-1}. For free carbonate ion, the bands are $v_a(CO_3^{2-})$ at 1450-1420 and $v_s(CO_3^{2-})$ at 1090-1020 cm^{-1}.[40,41] Based on the similar spectra for both fresh catalysts, adding spinel to the PGM-Only catalyst gives negligible change in the CO adsorption on Pt, as suggested by the very small peak shift for Pt-CO and CO-Pt-CO peaks.

Moving to the post-steam reforming scenarios, the spectra of both spent PGM-Only and PGM+Spinel catalysts after being treated with one steam reforming experiment are compared in Fig. 10b. Additionally, the PGM+Spinel catalyst sample that has been treated with three consecutive steam reforming runs as mentioned in section 3.3 was also analyzed using DRIFTS. Several differences in the spectra are observed in Fig. 10b. While the PGM-Only catalyst retains the two peaks at 2093 cm^{-1} (Pt-CO) and 2073 cm^{-1} (CO-Pt-CO), only one peak at 2073 cm^{-1} (CO-Pt-CO) with a smaller shoulder at higher wavenumber was detected for the PGM+Spinel catalyst. This reflects that fewer PGM sites may be available, which aligns with the steam reforming experiment results. Adsorbed bicarbonate species on Pt are also present on both PGM-Only and PGM+Spinel catalysts. The bands are v(CO) at 1640 or 1650, $v_a(COO)$ at 1435, 1470, or 1430, $v_s(COO)$ at 1304 and v(COH) at 1230 cm^{-1}.[42,43] In the lower wavenumber region, more intense band between 1430-1631cm^{-1} was detected for PGM+Spinel catalyst, which suggests strong bidentate carbonate, carbonate or bicarbonate adsorption. A new peak located between 1286-1452cm^{-1} was seen only in the PGM+Spinel catalyst. This band is assigned to the bicarbonate species on FeO_x, which was reported to have bands: $v_a(CO)$ at 1655-1615, $v_s(CO)$ at 1400-1370 and (δOH) at 1300 cm^{-1}.[44,45] Possible carbonate

species on MnO_x may present as well, which have peaks at 1494, 1418 and 1360 cm^{-1}.[46,47] The less detectable binding of CO on MnO_x compared to FeO_x is attributed to the small amount of Mn species detected during SEM-EDX characterization.

Similarly, bidentate carbonate, carbonate, bicarbonate species related to Pt, FeO_x and possibly MnO_x are evident in the PGM+Spinel sample after three steam reforming runs. For better comparison of the relative intensity between different samples, the spectra are normalized first such that the percentage of the transmittance values have the range of 0 to 1 (method of normalization shown in section 6, SI). Peaks with a low normalized value (low percentage of transmittance) suggest high intensity. The normalized spectra of PGM+Spinel samples are compared in Fig. 10c. For the PGM+Spinel sample with three steam reforming runs completed, the peak at 2096 cm^{-1} (Pt-CO) and 2077 cm^{-1} (CO-Pt-CO) are less intense, indicating less available PGM sites due to prolonged steam reforming treatment. Additionally, the ratio of CO-Pt-CO peak at ~2077 cm^{-1} to bicarbonate on FeOx peak at 1375 cm^{-1} of both samples is estimated to be 0.23 (1 run) and 0.89 (3 runs). The higher value reflects an increase of the Fe species or decrease of the available active sites on the PGM layer due to longer steam reforming treatment, which agrees with the SEM-EDX results. Additional normalized spectra of the PGM-Only and PGM+Spinel samples treated with different experimental conditions were provided and compared in the section 6, SI.

The SEM-EDX results suggest that the base metal and/metal oxide species migration from the spinel layer reduces the available PGM active sites. The CO-DRIFTS characterization is consistent with Fe species migration to the surface of the PGM layer of the PGM+Spinel catalyst. Thus, the aforementioned CH_4 conversion drop in the PGM+Spinel catalyst (30/60/15) with 15 g/L spinel loading can be explained by Fe and Mn migration to the PGM layer. The slow deactivation seen in Fig. 4b is likely a result of the slow migration of these species from the bottom to top layer. Finally, higher CH_4 conversion in the second and third steam reforming runs were achieved compared to the CH_4 conversion at the end of first run (Fig. 6). This may be related to the stability of the migrated species. The cooling or low temperature after the first and second run, may destabilize or modify the form of the surface species, such that the PGM activity is partially

recovered. The dynamic response of the PGM+MFO catalyst surface to changes in reaction conditions is very interesting and may be leveraged for dynamically operated catalytic systems, but its complexity warrants additional investigations that are outside the scope of this study.

3.5 Zoned catalyst design

With the understanding that MO_xH_x migration from MFO to the PGM layer blocks active sites and inhibits CH_4 steam reforming, a zoned catalyst design is proposed to decouple the CH_4 oxidation and reforming catalytic chemistries. The zoned catalyst configuration consists of an upstream dual-layer PGM+Spinel catalyst to accomplish the CH_4 oxidation, followed by a PGM-Only catalyst to accomplish the reforming. To examine this design, two different zoned catalysts (zoned catalyst #1 and #2) were prepared with the schematics shown in Fig. 11a. For zoned catalyst #1, small pieces of the PGM+Spinel (30/100/25) and PGM-Only (30/100a) monolith samples are arranged end-to-end with the PGM+Spinel piece in the front and the PGM-Only piece in the back. Each monolith piece has the same diameter and length, and the combined dimension of the zoned catalyst is 1" (L) and 0.85" (D). Compared to the PGM+Spinel (30/100/25) catalyst, zoned catalyst #1 has the overall spinel loading reduced from 25 g/L to 12.5 g/L. For zoned catalyst #2, small pieces of PGM+Spinel (30/140/35) the PGM-Only (30/100a) monolith samples are placed in the front and back, respectively. The PGM+Spinel (30/140/25) piece has the dimension of 0.65" (L) and 0.85" (D); the PGM-Only (30/100a) piece has the dimension of 0.35" (L) and 0.85" (D). Compared to the PGM+Spinel (30/140/35) catalyst, zoned catalyst #2 has an overall spinel loading reduced from 35 g/L to 12.25 g/L. The two zoned catalysts were designed such that the overall PGM loading is fixed at 30 g/ft^3 but with similar overall spinel loadings of 12.5 g/L and 12.25 g/L. The performances of the zoned catalysts were compared to that of the PGM+Spinel (30/60/15) catalyst, which has the same PGM loading and a similar spinel loading at 15 g/L.

CH_4 conversion profiles were compared under both time-invariant (Fig. 11b) and modulated full feeds (Fig. 11c). With the modulated feed, the CH_4 light-off curves of the PGM+Spinel (30/60/15) catalyst and zoned catalyst #1 overlap up to ~70% CH_4 conversion, but the zoned catalyst design outperforms the PGM+Spinel catalyst in the

higher temperature range of 410ºC to 532ºC. The O_2 profile of the zoned catalyst (shown in Fig. S5 in section 5 of the SI) reveals that CH_4 steam reforming occurs within this temperature range. Similar trends were observed for the time-invariant feed. The enhanced CH_4 steam reforming activity of the zoned catalyst #1 suggests that the absence of spinel in the back of the catalyst reduces the detrimental effect of spinel on reforming activity while retaining the promotional effect of the spinel on the oxidation activity. While the spatial reaction profile along the monolith is not known, a front oxidation zone and a back reforming zone is likely to exist, following the earlier work of Bugosh et al.[9] The CH_4 profile of the zoned catalyst #1, however, overlaps with the CH_4 profile of the PGM+Spinel catalyst at temperature above 532ºC. The higher temperature likely mobilizes more MO_xH_y species that block PGM sites, rendering the zoned design of catalyst #1 ineffective. To further increase the CH_4 conversion at high temperature, zoned catalyst #2 with a shorter front spinel containing zone and a longer back PGM-Only zone was tested. At high temperature, further enhancement compared to zoned catalyst #1 was achieved with 97% and 96% CH_4 conversions under modulated and time-invariant feed conditions, with respectively. The O_2 profiles in Fig. S4 indicate that O_2 depletes at 370ºC (modulated feed) and at 440ºC (time-invariant feed). After O_2 depletion, the higher CH_4 conversion observed suggests the enhanced SRM activity of the zoned catalyst #2. The high temperature enhancement is explained by the longer PGM-Only zoned at the back, thus lessening the detrimental impact from the base metal species migration.

In the lower temperature regime, zoned catalyst #2 also exhibits a shift of the CH_4 light-off temperature (T_{50}) to lower temperature. This is attributed to enhanced CH_4 oxidation activity by the increased spinel loading in the front zone. While the three catalysts have a similar overall spinel loading, zoned catalyst #2 has a higher spinel loading in the front 0.35'' length compared to zoned catalyst #1 and the PGM+Spinel catalyst. The correlation of T_{50} and spinel loading are shown Figs. S7a and S7b. Under both modulated and time-invariant feed conditions, PGM+Spinel (30/140/35) catalyst, which has the highest spinel loading, give the lowest T_{50} values. The increased spinel loading provides more available spinel for excess O_2 removal under lean conditions, thus leaving more available active PGM sites for CH_4 oxidation reaction. However, at high temperature, the PGM+Spinel (30/140/35) catalyst has limited CH_4 conversions at 92% and 89% under modulated feed

and time-invariant feed, respectively. The lower CH_4 conversion at high temperature compared to the PGM-Only catalyst was again attributed to the base metal migration issue. While the proposed zoned catalyst design was not able to fully eliminate the detrimental impact of spinel at high temperatures, it gives some insights on the optimization of the catalyst composition profile.

4 Conclusions

The CH_4 conversion activity of a $Pt+Pd/Al_2O_3$ monolith catalyst with the addition of $Mn_{0.5}Fe_{2.5}O_4$ (MFO) spinel was examined through flow experiments under both time-invariant and modulated feed conditions. The enhanced CH_4 oxidation activity under lean/rich feed modulation at lower temperature is attributed to the more active, dynamically formed PGM active sites for CH_4 dissociation. The addition of MFO spinel to the PGM catalyst mitigates O_2 inhibition through O_2 diffusion to and removal by the spinel layer and, in turn, retaining a more active PGM surface in a partially oxidized state for enhanced CH_4 activation. The removal of SRM and partial oxidation products CO and H_2 during modulation is an additional process that will be examined in a forthcoming publication. At high temperature, the PGM-Only catalyst outperforms the PGM+Spinel catalyst, achieving full CH_4 conversion via CH_4 steam reforming after O_2 is depleted. SRM experiments confirm a significant drop in CH_4 conversion when MFO spinel was added to the PGM-Only catalyst. Thus, a steam reforming study was conducted to investigate the cause of the detrimental impact of spinel on SRM activity. Based on catalyst characterization on pre- and post-steam reforming catalysts through SEM-EDX, base metal and/metal oxide species migration, primarily Fe, from the spinel layer to the PGM layer occurred during CH_4 steam reforming reaction, leading to a loss of active PGM sites. DFT calculations confirm the favorable thermodynamics of FeO_xH_y migration, blocking of Pt(211) step sites and even complete encapsulation of Pt. DRIFTS experiment using CO as probe molecule are consistent with surface Fe species on the PGM-layer. A zoned catalyst design with spinel loading confined in the front part of the monolith catalyst is proposed and shown to combine CH_4 oxidation benefits below 400 °C with increased CH_4 steam reforming activity above 410ºC under modulated reaction conditions.

CONFLICTS OF INTEREST

There are no conflicts to declare.

REFERENCES

1 F. Huang, J. Chen, W. Hu, G. Li, Y. Wu, S. Yuan, L. Zhong and Y. Chen, *Appl. Catal., B*, 2017, **219**, 73–81.

2 P. Gélin and M. Primet, *Appl. Catal., B*, 2002, **39**, 1–37.

3 Y. Chang and J. G. McCarty, *Catal. Today*, 1996, **30**, 163–170.

4 S. Golden, Z. Nazarpoor and M. Launois, *SAE Technical Paper*, 2015, 2015-01-1007.

5 D. Ferri, M. Elsener and O. Kröcher, *Appl. Catal., B*, 2018, **220**, 67–77.

6 S. B. Kang, K. Karinshak, P. W. Chen, S. Golden and M. P. Harold, *Catal. Today*, 2021, **360**, 284–293.

7 J. Gong, J. Pihl, D. Wang, M. Kim, W. P. Partridge, J. Li, M. Cunningham, K. Kamasamudram, N. Currier and A. Yezerets, *Catal. Today*, 2021, **360**, 294–304.

8 G. S. Bugosh, V. G. Easterling, I. A. Rusakova and M. P. Harold, *Appl. Catal., B*, 2015, **165**, 68–78.

9 M. Salaün, A. Kouakou, S. Da Costa and P. Da Costa, *Appl. Catal., B*, 2009, **88**, 386–397.

10 G. Kresse and J. Hafner, *Phys. Rev. B*, 1993, **47**, 558–561.

11 G. Kresse and J. Hafner, *Phys. Rev. B*, 1994, **49**, 14251–14269.

12 G. Kresse and J. Furthmüller, *Phys. Rev. B*, 1996, **54**, 11169–11186.

13 G. Kresse and J. Furthmüller, *Comput. Mater. Sci.*, 1996, **6**, 15–50.

14 S. R. Bahn and K. W. Jacobsen, *Comput. Sci. Eng.*, 2002, **4**, 56–66.

15 P. E. Blöchl, *Phys. Rev. B*, 1994, **50**, 17953–17979.

16 G. Kresse and D. Joubert, *Phys. Rev. B*, 1999, **59**, 1758–1775.

17 J. Wellendorff, K. T. Lundgaard, A. Møgelhøj, V. Petzold, D. D. Landis, J. K. Nørskov, T. Bligaard and K. W. Jacobsen, *Phys. Rev. B*, 2012, **85**, 235149.

18 W. P. Davey, *Phys. Rev.*, 1925, **25**, 753–761.

19 L. Bengtsson, *Phys. Rev. B*, 1999, **59**, 12301–12304.

20 H. C. Galloway, J. J. Benitez and M. Salmeron, *Surf. Sci.*, 1993, **298**, 127–133.

21 J. Knudsen, L. R. Merte, L. C. Grabow, F. M. Eichhorn, S. Porsgaard, H. Zeuthen, R. T. Vang, E. Lægsgaard, M. Mavrikakis and F. Besenbacher, *Surf. Sci.*, 2010, **604**, 11–20.

22 Z.-H. Qin, M. Lewandowski, Y.-N. Sun, S. Shaikhutdinov and H.-J. Freund, *J. Phys. Chem. C*, 2008, **112,** 10209–10213.

23 P. Carlsson, E. Fridell and M. Skoglundh, *Catal. Lett.*, 2007, **115**, 1–7.

24 S. Fouladvand, M. Skoglundh and P. Carlsson, *Catal. Sci. Technol.*, 2014, **4**, 3463–3473.

25 I. Y. Pakharukov, I. P. Prosvirin, I. A. Chetyrin, V. I. Bukhtiyarov and V. N. Parmon, *Catal. Today*, 2016, **278**, 135–139.

26 I. Y. Pakharukov, A. Y. Stakheev, I. E. Beck, Y. V. Zubavichus, V. Y. Murzin, V. N. Parmon and V. I. Bukhtiyarov, *ACS Catal.*, 2015, **5**, 2795–2804.

27 Y. H. Chin, C. Buda, M. Neurock and E. Iglesia, *J. Am. Chem. Soc.*, 2011, **133**, 15958–15978.

28 E. Becker, P. Carlsson and M. Skoglundh, *Top. Catal.*, 2009, **52**, 1957–1961.

29 G. Jones, J. G. Jakobsen, S. S. Shim, J. Kleis, M. P. Andersson, J. Rossmeisl, F. Abild-Pedersen, T. Bligaard, S. Helveg, B. Hinnemann, J. R. Rostrup-Nielsen, I. Chorkendorff, J. Sehested and J. K. Nørskov, *J. Catal.*, 2008, **259**, 147–160.

30 J. Wei and E. Iglesia, *J. Phys. Chem. B*, 2004, **108**, 4094–4103.

31 V. B. Mortola, S. Damyanova, D. Zanchet and J. M. C. Bueno, *Appl. Catal., B*, 2011, **107**, 221–236.

32 M. Adamowska and P. Da Costa, *J. Nanopart.*, 2015, Article ID 601941.

33 H. Chadwick, H. Guo, A. Gutiérrez-González, J. P. Menzel, B. Jackson and R. D. Beck, *J. Chem. Phys.*, 2018, **148**, 014701.

34 Y. Chen and D. G. Vlachos, *Ind. Eng. Chem. Res.*, 2012, **51**, 12244–12252.

35 L. R. Merte, J. Knudsen, F. M. Eichhorn, S. Porsgaard, H. Zeuthen, L. C. Grabow, E. Lægsgaard, H. Bluhm, M. Salmeron, M. Mavrikakis and F. Besenbacher, *J. Am. Chem. Soc.*, 2011, **133**, 10692–10695.

36 K. I. Hadjiivanov and G. N. Vayssilov, *Adv. Catal.*, 2002, **47**, 307–511.

37 F. Zaera, *Chem. Soc. Rev.*, 2014, **43**, 7624–7663.

38 C. M. Kalamaras, G. G. Olympiou and A. M. Efstathiou, *Catal. Today*, 2008, **138**, 228–234.

39 D. W. Daniel, *J. Phys. Chem.*, 1988, **92**, 3891–3899.

40 M. J. Hazlett, M. Moses-Debusk, J. E. Parks II, L. F. Allard and W. S. Epling, *Appl. Catal., B*, 2017, **202**, 404–417.

41 Z. Li, Y. Geng, L. Ma, X. Chen, J. Li, H, Chang and J. W. Schwank, *Front. Environ. Sci. Eng.*, 2020, **14**, 65.

42 M. J. Hazlett and W. S. Epling, *Catal. Today*, 2016, **267**, 157–166.

43 G. Busca, E. Finocchio and V. S. Escribano, *Appl. Catal., B*, 2012, **113-114**, 172–179.

44 J. A. Loiland, M. J. Wulfers, N. S. Marinkovic and R. F. Lobo, *Catal. Sci. Technol.*, 2016, **6**, 5267–5279.

45 G. Busca and V. Lorenzelli, *J. Mater. Chem.*, 1982, **7**, 89–126.

46 X. Zhang, Y. Deng, P. Tian, H. Shang, J. Xu and Y. Han, *Appl. Catal., B*, 2016, **191**, 179–191.

47 W. Yang, Z. Su, Z. Xu, W. Yang, Y. Peng and J. Li, *Appl. Catal., B*, 2020, **260**, 118150.

48 J. Towns, T. Cockerill, M. Dahan, I. Foster, K. Gaither, A. Grimshaw, V. Hazlewood, S. Lathrop, D. Lifka, G. D. Peterson, R. Roskies, J. R. Scott and N. Wilkins-Diehr, *Comput. Sci. Eng.*, 2014, **16**, 62–74.

Table 1. Summary of monolith catalysts used in this study

Monolith catalysts	Architecture	PGM loading (g/ft^3)	Spinel loading (g/L)
PGM-Only 30/100a, 30/60a	PGM top layer (100 g/L) Al$_2$O$_3$ bottom layer (100, 60 g/L)	30 [a]	0
Spinel-Only 0/100/25, 0/60/15	Spinel layer (100, 60 g/L)	0	25 [b], 15 [b]
PGM+Spinel 30/140/35, 30/100/25, 30/60/15, 30/60/11.25, 30/60/7.5	PGM top layer (100 g/L) Spinel bottom layer (140, 100, 60 g/L)	30 [a]	35 [b], 25 [b], 15 [b] 11.25 [c], 7.5 [d]
PGM+Spinel 30/100/25-PM	Single layer (200 g/L)	30 [a]	12.5

[a] Pt:Pd-19:1/Al$_2$O$_3$

[b] Mn$_{0.5}$Fe$_{2.5}$O$_4$ spinel layer (140, 100, 60 g/L) composition: 25 wt% spinel/ 75 wt% Al$_2$O$_3$

[c] Mn$_{0.5}$Fe$_{2.5}$O$_4$ spinel layer (60 g/L) composition: 18.75 wt% spinel/ 81.25 wt% Al$_2$O$_3$

[d] Mn$_{0.5}$Fe$_{2.5}$O$_4$ spinel layer (60 g/L) composition: 12.5 wt% spinel/ 87.5 wt% Al$_2$O$_3$

Table 2. Feed compositions used in this study

Species [a]	Complex feed, time-invariant	Complex feed, modulated	Steam reforming
	$\lambda = 0.992$	$\lambda_{avg} = 0.992$ (0.978~1.006 at 0.33 Hz)	
CH_4	1500 ppm	1500 ppm	1500 ppm
CO	8000 ppm	8000 ppm	0
H_2	1000 ppm	1000 ppm	0
NO	1000 ppm	1000 ppm	0
O_2	5650 ppm	3400 ppm ~ 7900 ppm	0
H_2O	10 %	10 %	10 %
CO_2	10 %	10 %	0

[a] N_2 balance
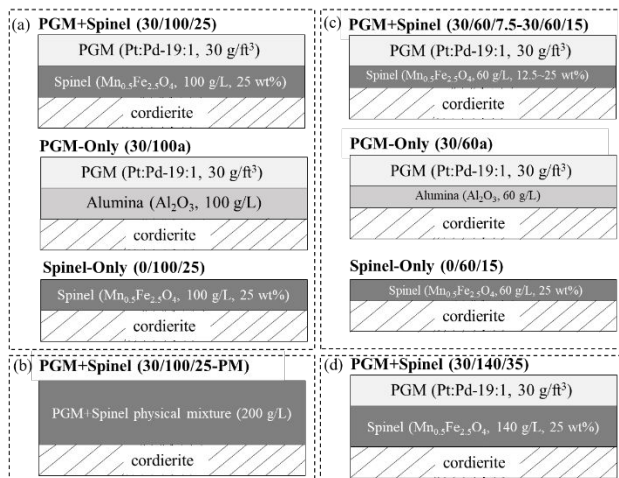
Fig. 1. (a) Three types of washcoated monolith samples [PGM and spinel layer thickness: 1.64 g/in^3]; **(b)** single-layer PGM+Spinel monolith sample; **(c)** three types of washcoated monolith samples with varying spinel loadings [PGM layer thickness: 1.64 g/in^3; spinel layer thickness: 0.98 g/in^3]; **(d)** PGM+Spinel monolith sample [PGM layer thickness: 1.64 g/in^3; spinel layer thickness: 2.30 g/in^3].
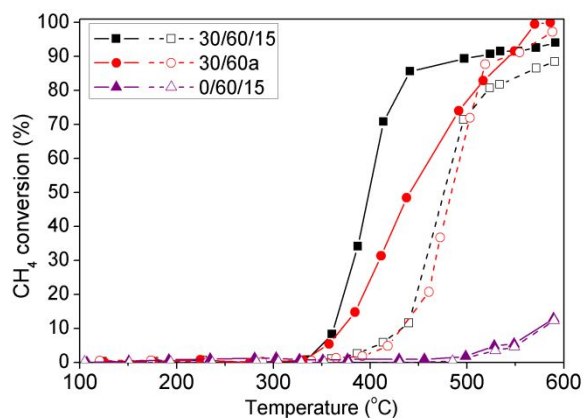
Fig. 2. CH$_4$ conversion under modulated [filled symbols] and time-invariant [unfilled symbols] feeds.
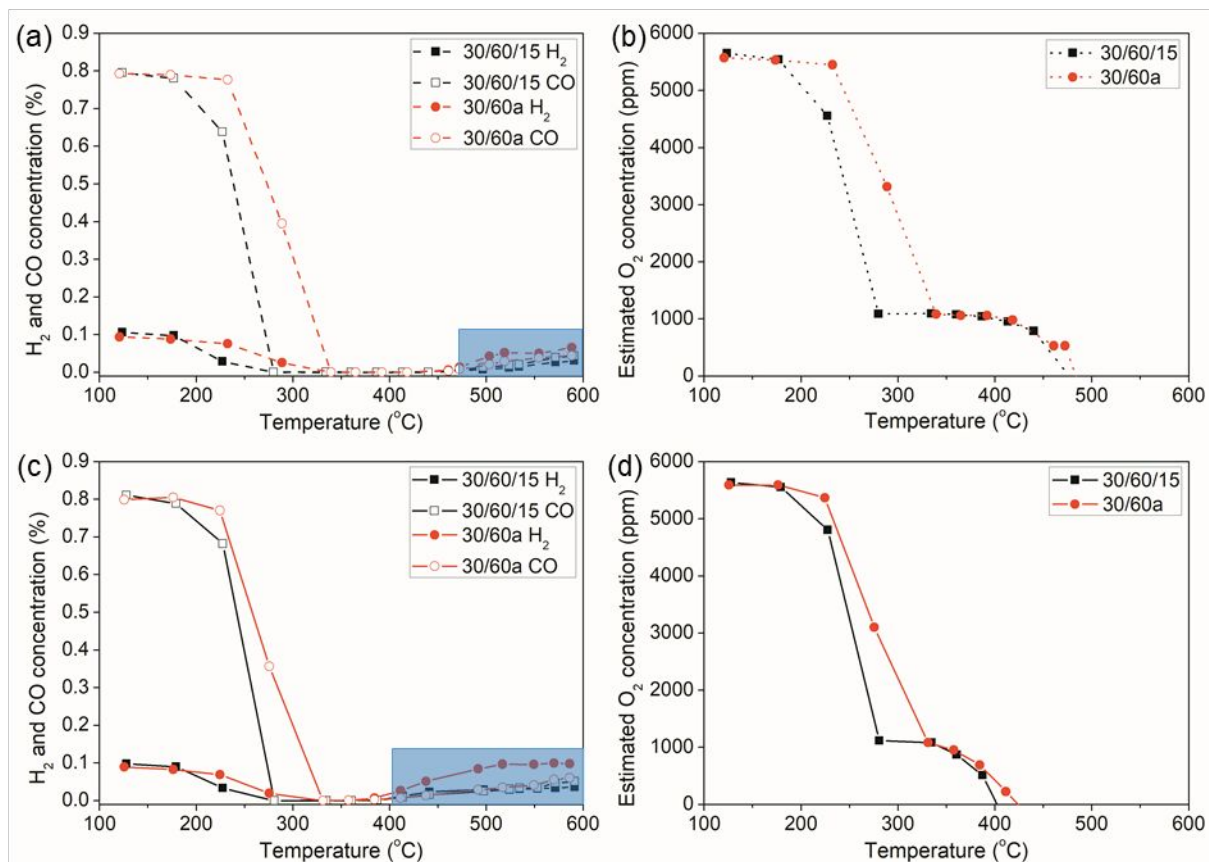
Fig. 3. CO and H$_2$ effluent concentrations under full **(a)** time-invariant feed and **(c)** modulated feed (blue shade highlighting formation of CO and H$_2$); estimated O$_2$ concentration under full **(b)** time-invariant feed and **(d)** modulated feed.
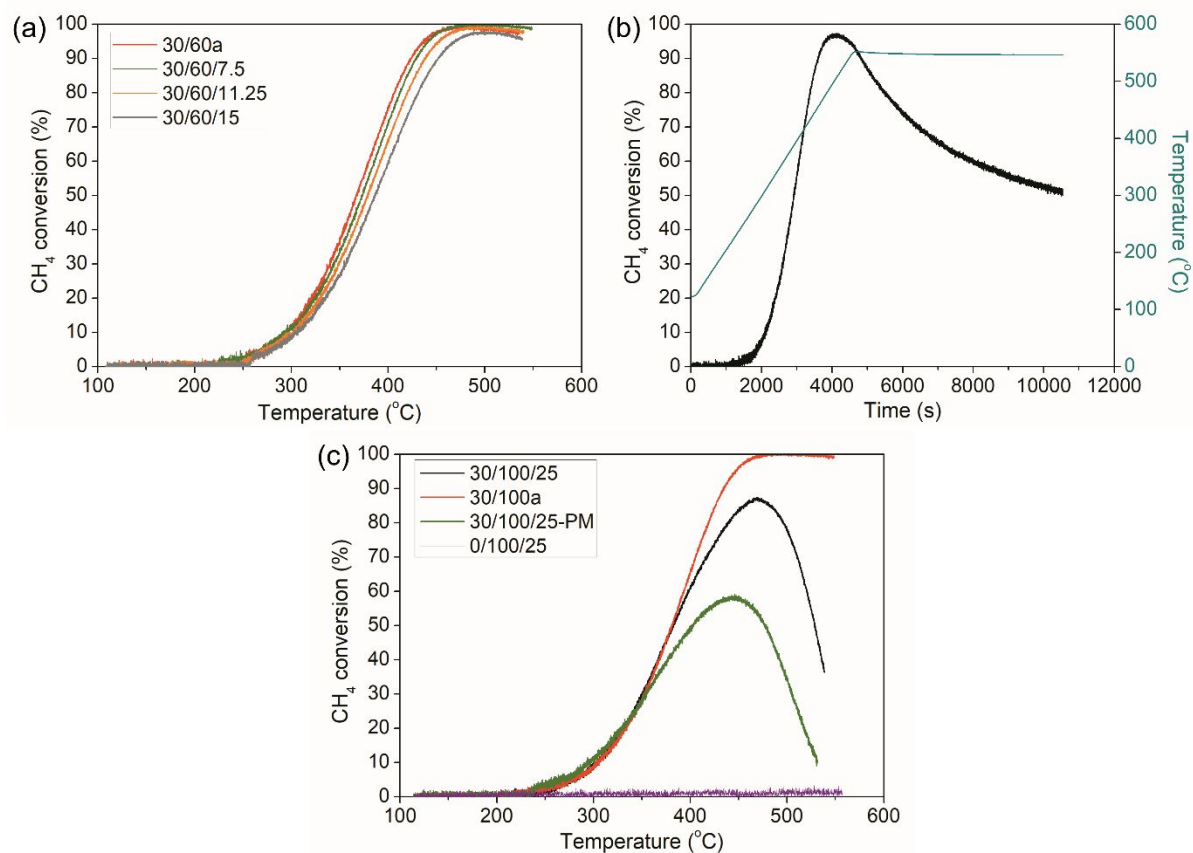
Fig. 4. CH$_4$ steam reforming activity over **(a)** PGM+Spinel catalysts with different spinel loadings and **(b)** PGM+Spinel (30/60/15) catalyst; **(c)** PGM-Spinel proximity effect on CH$_4$ steam reforming activity.
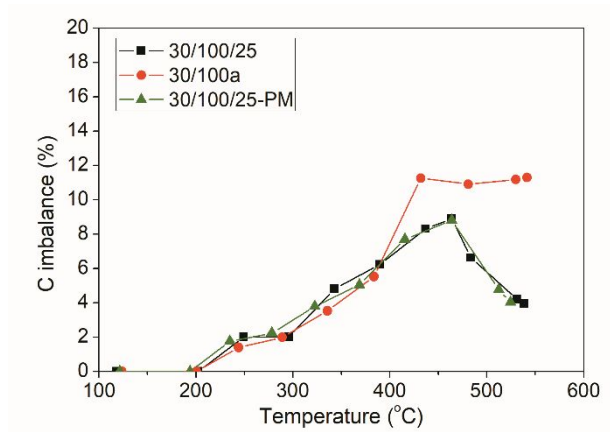
Fig. 5. Calculated C imbalances at selected temperatures during CH$_4$ steam reforming experiment.
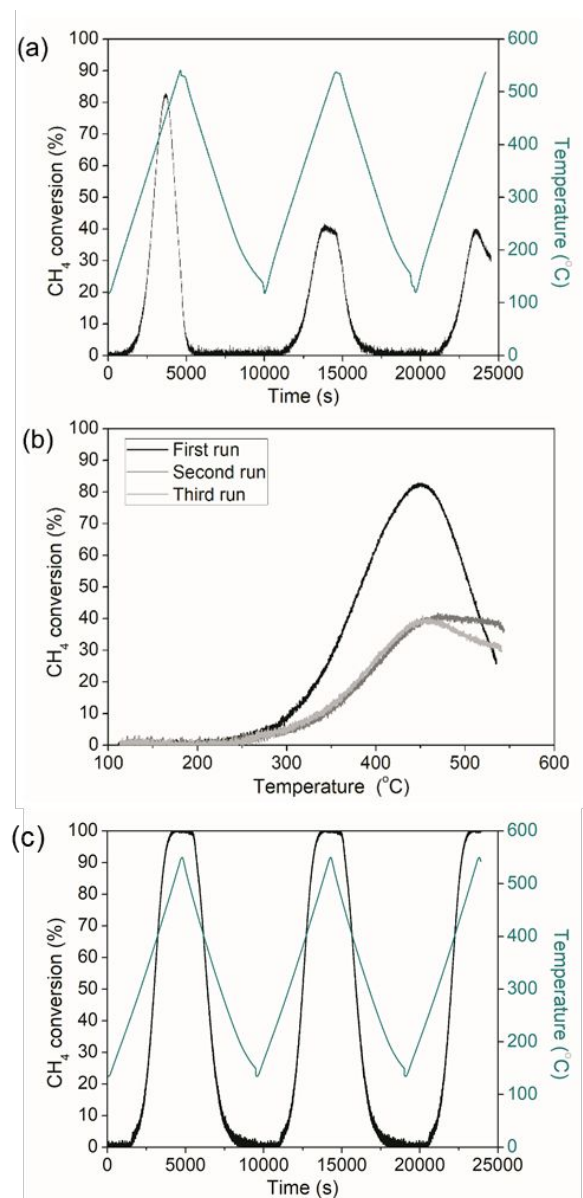
Fig. 6. CH$_4$ conversion over PGM+Spinel (30/100/25) in three consecutive steam reforming runs **(a)** plotted versus time and **(b)** plotted versus temperature; **(c)** CH$_4$ conversion over PGM-Only (30/100a) in three consecutive steam reforming runs.

(a) Fresh 30/100/25   30/100/25 (1 SR run)   30/100/25 (3 SR runs)

(b)
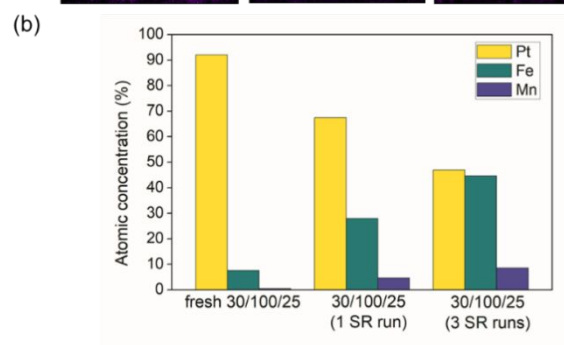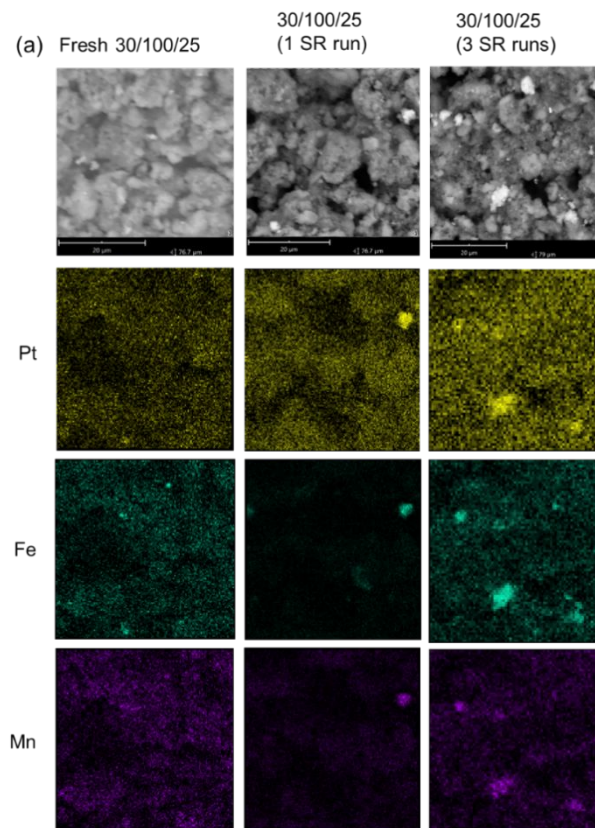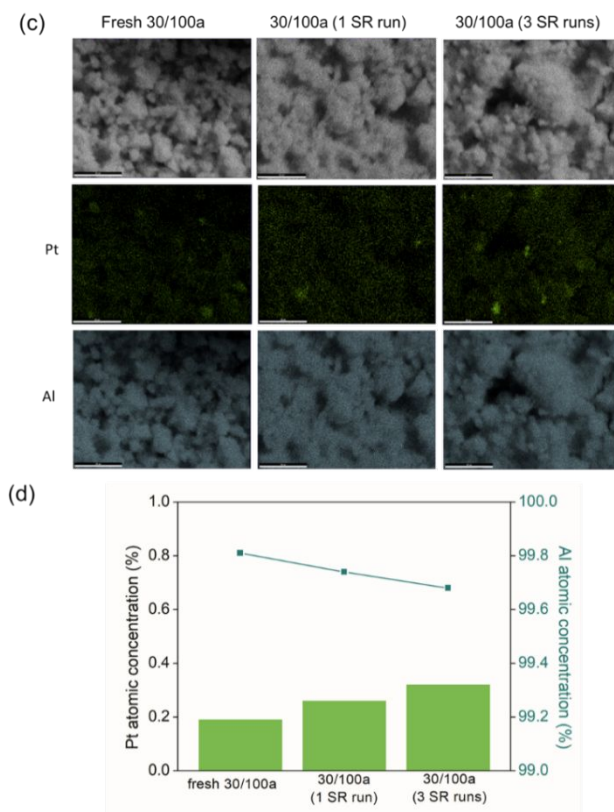
Fig. 7. (a) SEM images and area mappings on elements Pt (yellow), Fe (teal) and Mn (purple); **(b)** measured average atomic concentrations of Pt, Fe and Mn; **(c)** SEM images and area mappings on elements Pt (green) and Al (light blue); **(d)** measured average atomic concentrations of Pt and Al.
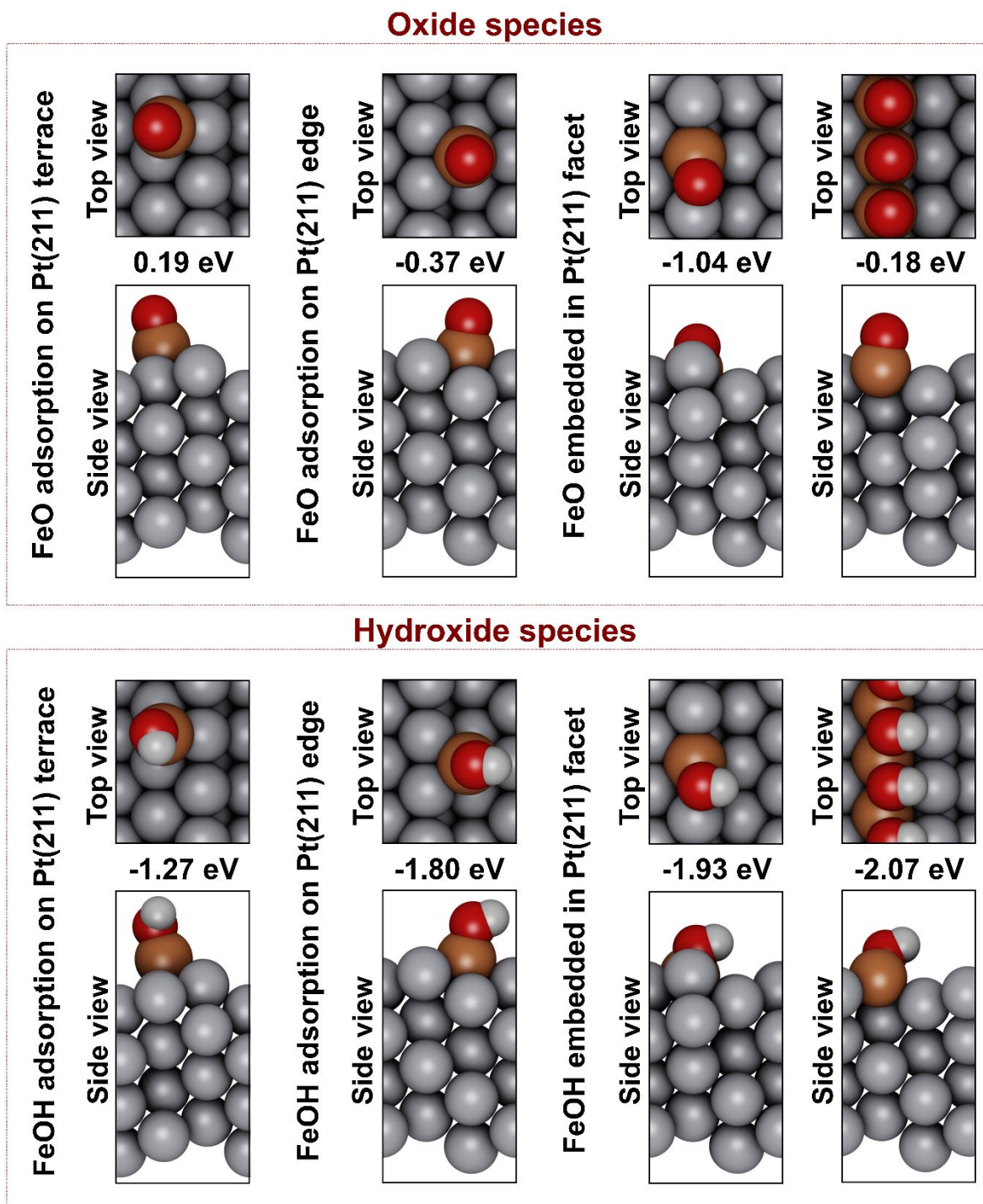
Fig. 8. Top panel: Energy of adsorption of monomers and linear chains of FeO species on the step site of Pt(211). Lower panel: Energy for embedding monomers and linear chains of FeOH species in Pt(211) steps.
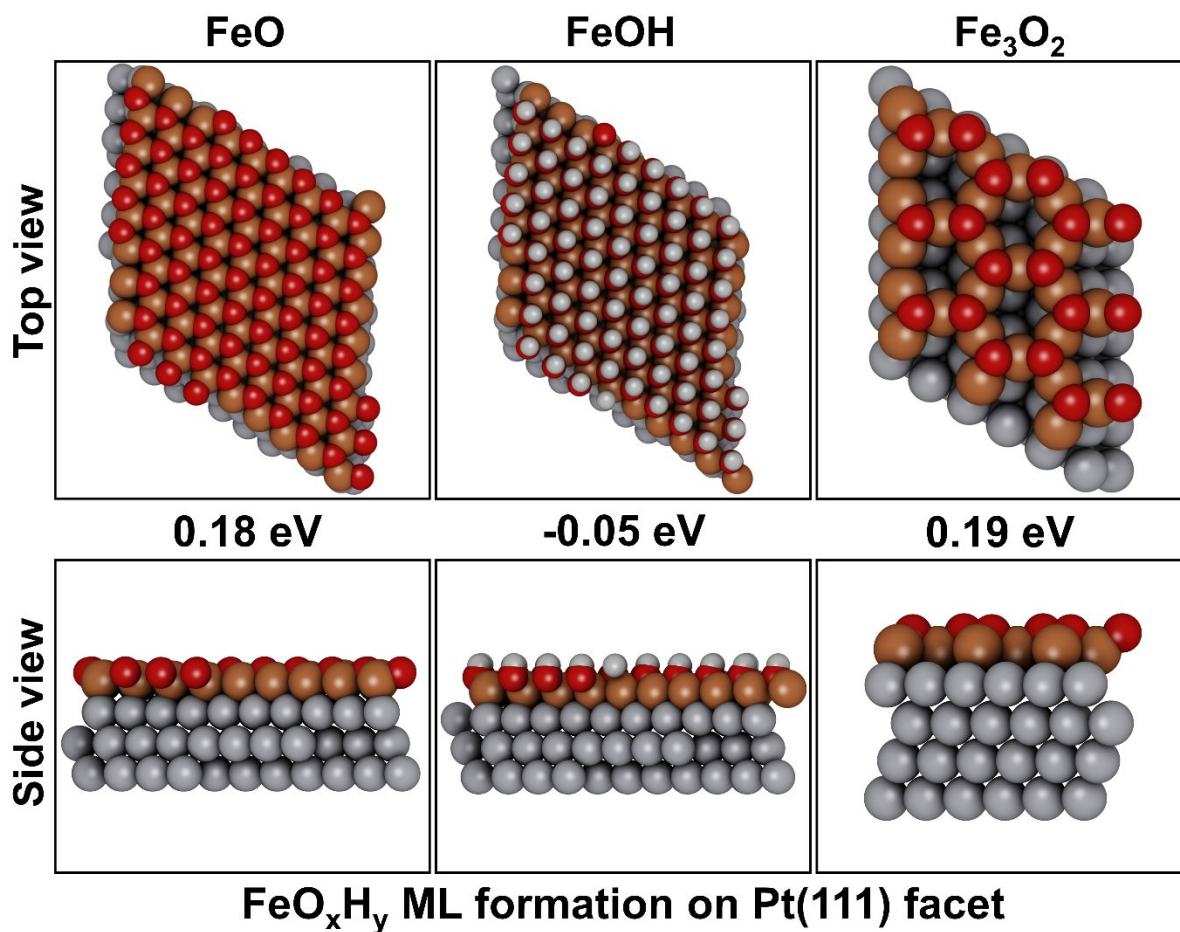
FeOₓHᵧ ML formation on Pt(111) facet

Fig. 9. Energy of formation of FeOₓHᵧ overlayers on Pt(111). For reduced iron oxide (Fe₃O₂) on Pt(111), the energy of adsorption was calculated as:

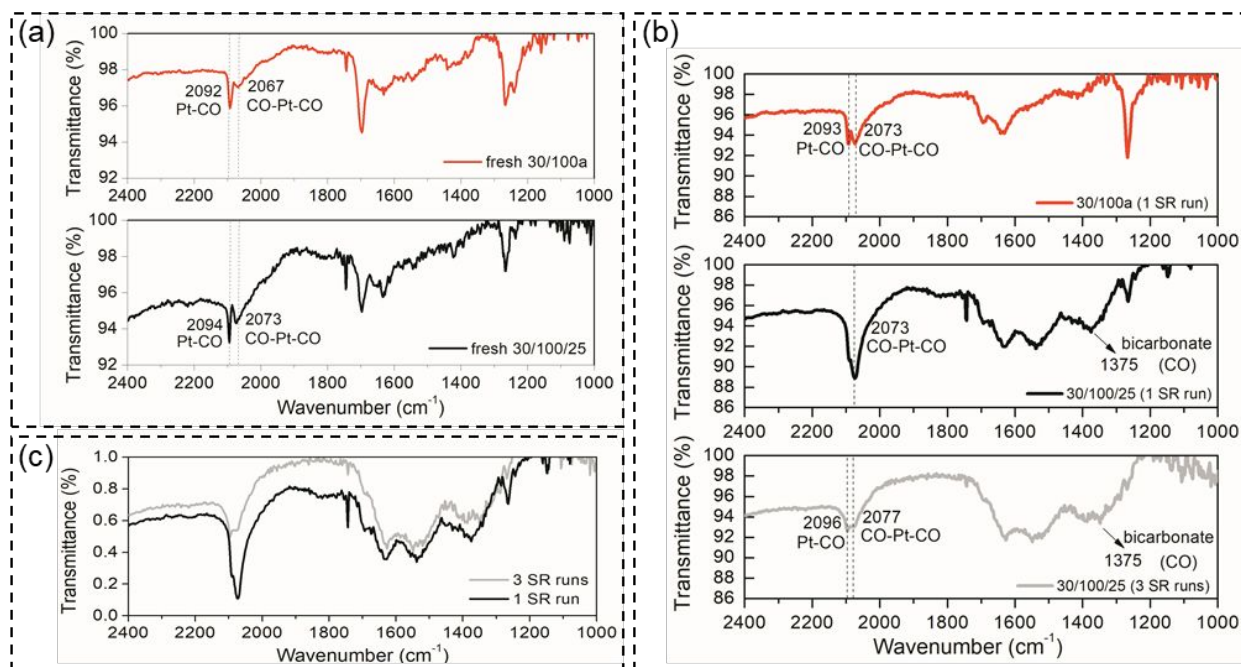$$3 \times E_{ads} = E[Fe_3O_2 \; on \; Pt(111)] - E[Pt(111)] - 3 \times E[FeO(bulk)] + E[CO_2] - E[CO].$$

Fig. 10. DRIFTS spectra collected during Ar purge over **(a)** fresh catalysts and **(b)** PGM-Only (1 steam reforming run), PGM+Spinel (1 steam reforming run and 3 steam reforming runs); **(c)** normalized DRIFTS spectra on PGM+Spinel catalyst (1 and 3 steam reforming runs).
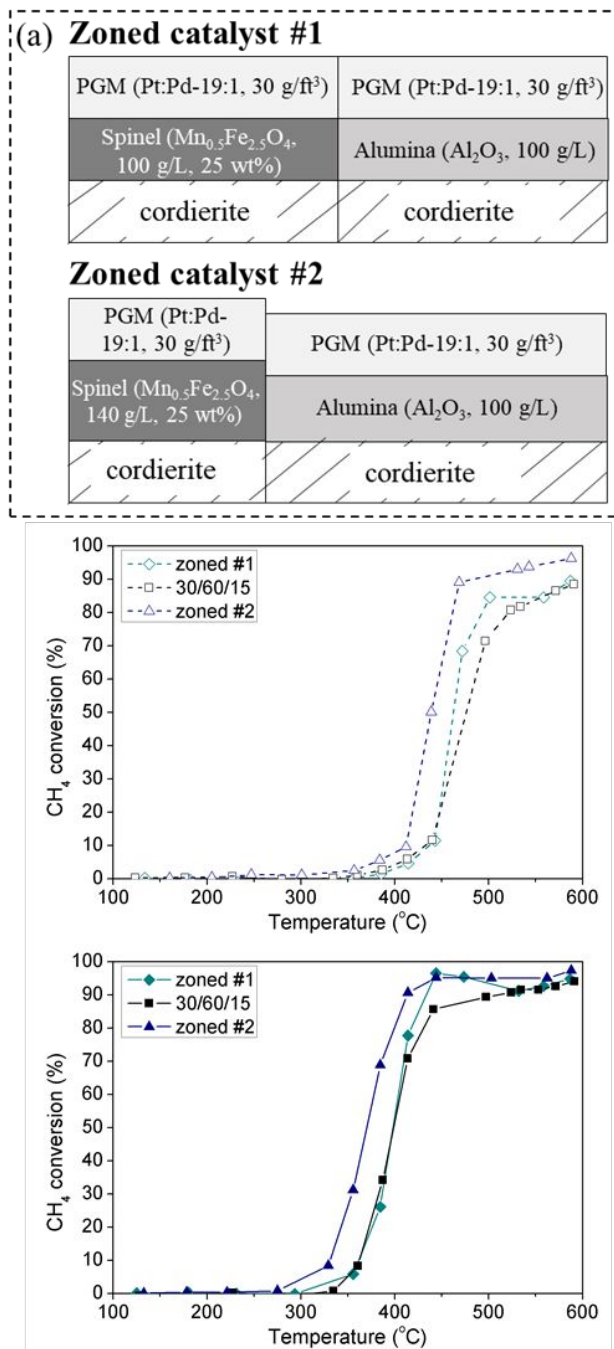
Fig. 11. (a) Schematic of zoned catalyst #1 and #2; CH$_4$ conversion profiles of PGM+Spinel (30/60/15) catalyst, zoned catalyst #1 and #2 under **(b)** time-invariant feed [unfilled symbols] and **(c)** under modulated feed [filled symbols].